



Final Project Report

Alberta Upstream Research Petroleum Fund (AURPF)

Potential Release of Additives used in the Hydraulic Fracturing Process into the Atmosphere

Authors:

Mohsen Kazemimanesh, Alireza Moallemi, A. Melina Jefferson, Darcy J. Corbin, Alireza Vali,
Matthew R. Johnson, Larry W. Kostiuk, Jason S. Olfert

Edmonton, Alberta

December 2016

Executive Summary

The objectives of this project were to i) complete a literature review of the composition of flowback of conventional and unconventional wells, ii) design, build, and test a small scale flame and sampling system to enable future work investigating particle formation mechanisms in flames with flowback droplets, and iii) large scale experiments to investigate the effect of flowback droplets on flare efficiency.

Extensive compositional data of flowback and produced water (water produced by the well after the production process has started) is available from thousands of conventional and unconventional well sites through a database maintained by the U.S. Geological Survey. Anions found in high concentrations in the flowback water include (listed in order of decreasing concentration) Cl^- , CHO_3^- , and SO_4^{2-} , with Cl^- having orders of magnitude higher concentrations than the other anions. Common cations include: Na^+ , Ca^{2+} , K^+ , and Mg^{2+} . Data analysis on the USGS data showed that conventional hydrocarbon wells has the highest median concentration of cations and chlorine. This is likely due to the fact that the produced water from conventional hydrocarbon wells is mostly brine water and it is not diluted with fresh water from the fracturing process. Furthermore, for unconventional wells, the lowest concentrations of cations and chlorine are found at the beginning of flowback and they slowly increase in concentration with respect to time as flowback continues.

In the small-scale experiment, nanoparticles generated by a laminar methane jet diffusion flame were characterized by direct sampling through the pinhole of a probe and sized with a nano-scanning mobility particle sizer. Particular attention was paid to verify the validity of the probe-sampling technique. Results showed that the particle size distributions (PSD) were strongly affected by sample dilution immediately after extraction. Within the flame, the soot PSD did not become independent of dilution ratio until the sample was diluted several thousand times (depending on initial concentration) within a few milliseconds of extraction.

High spatially resolved experimental results at different heights (typically 1 mm apart) along the central axis of the flame showed the evolution of PSD for particles larger than 2 nm covering early nucleation and growth to oxidation regions. Moving upward from the fuel-side, prior to the visible flame, the PSD in the particle nucleation region was bimodal (with one of the modes being smaller than 2 nm) and gradually turned into a unimodal PSD with a median of 10 nm due to particle growth. Nearer to the visible flame, the PSD became bimodal again with the larger-diameter mode growing in magnitude and being made up of ever-larger particles, while the smaller-diameter mode gradually shrunk in size until it vanished. Eventually, as the flow was leaving the visible flame, all the particles gradually oxidized until at the tip of the flame they reached a median diameter of 9 nm and in very low concentrations. This work will enable future work in the FlareNet project investigating particle formation mechanisms in flames with flowback droplets.

In the lab-scale experiment, fuel gas comprised of methane, propane, and butane in a mixture representative of upstream oil and gas products in western Canada was burned at atmospheric pressure. At the base of the flame, liquid aerosols were injected into the flare gas stream using an

atomizing system, which is capable of delivering consistently-sized droplets at flow rates of up to approximately 60 mL/min. The methodology to evaluate species yields and combustion efficiency is based on capturing the whole product plume and fully mixing it prior to sampling. The effects of injected liquid aerosols will be discussed in terms of prominent combustion product emission trends for various liquid loadings and solution strengths. Key results were: CO had a non-monotonic response to increasing levels of salt water injection, and emission trends with hydrochloric acid solutions were remarkably similar to distilled water.

Table of Contents

1	Background.....	1
1.1	Hydraulic fracturing and hydrofracturing fluid.....	1
1.2	Flowback and Produced Water	2
2	Chemical compound of a representative produced water solution.....	3
2.1	Methodology	3
2.1.1	Categorization of Produced Water Samples	3
2.1.2	Prominent species in the produced water samples.....	4
2.1.3	Dataset Generation Based on Regions and Formations.....	4
2.2	Results	5
2.3	Discussion	8
3	Small-scale diffusion flame experiment	9
3.1	Experimental setup.....	10
3.1.1	Co-flow burner.....	10
3.1.2	Sampling system.....	11
3.1.3	Particle measurement suite	12
3.1.4	Dilution ratio measurement.....	12
3.2	Results and discussion.....	13
3.2.1	Effect of dilution on particle size distribution	13
3.2.2	Effect of pinhole clogging on particle size distribution.....	14
3.2.3	Evolution of particle size distribution in the flame.....	15
3.3	Conclusions	17
4	Lab-scale turbulent flame experiment	18
4.1	Methodology	19
4.2	Results	20
4.3	Conclusions	22
5	Recommendations and Applications.....	22
	References.....	24

1 Background

1.1 Hydraulic fracturing and hydrofracturing fluid

Production of natural gas has rapidly increased alongside the widespread use of hydraulic fracturing (“fracturing”) as a means of securing non-traditional gas reserves, such as coal-bed methane and tight gas [1]. As the name suggests, fracturing is the process of injecting high-pressure (5-10,000 psi [2]) particulate and liquid mixtures into deep wells (4-12 km deep [3]) to create fractures in the bedrock (see Figure 1.1). The particulate, referred to as proppant, holds the fractures open to increase gas release from new or existing wells. Fracturing operations typically include flushing wells with high pressure acid (often 2-28% hydrochloric acid solution) followed by fracturing fluid and additional water and particulate mixtures [3–7]. It is also common that in addition to a pre-fluid acid wash, hydrochloric acid could be injected before each injection stage. Prior to well operation, flowback fluid (the liquid mixtures removed from wells) is recovered over a period of days to several months [8,9]. Flowback is sent to separation tanks [10] then to open holding tanks for eventual treatment or reuse, injection into depleted wells, or land disposal [4] depending on local regulations [11]. Directive 060 from the Alberta Energy Regulator (AER) requires all flowback to be separated by phase, and all droplets larger than 300 μm be removed from the gas component [12]. The gas stream is then directed to a flare, vented, or ‘green-completed’ (i.e., connected to an existing pipeline) [10,12]. The gas recovered from the separation tanks is vented to atmosphere or flared. Recent regulations have promoted flaring over venting [12].

Compositions of fracking fluids are generally not publicly disclosed due to their proprietary nature. Often corporations purchase ‘off the shelf’ chemical compounds from third parties who hold the

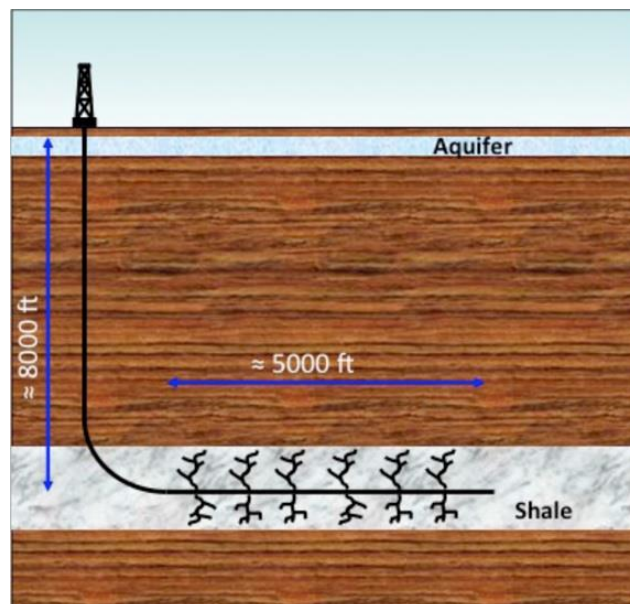


Figure 1.1. A demonstration of hydraulic fracturing in a horizontal wellbore [14].

rights to exact compositions [4,6,8,13]. A typical water-based mixture may include: biocides, surfactants, proppants (primarily sand), scale-inhibitors, acids (hydrochloric acid), breakers (used to reduce viscosity of fluids), and a variety of other chemicals used to alter the properties of the mixture to suit geological and well-type requirements [3,4,6,8,13].

1.2 Flowback and Produced Water

The flow returning from the well is either categorized as “flowback water” or “produced water”. Flowback water is the fluid which would return immediately after the hydraulic fracturing of the well with a high flow rate. Flowback water can return to the surface days or weeks after the hydraulic fracturing process. Produced water is the fluid returning to the surface after the production process of the well has started [14]. The flow returning from the well has a high concentration of inorganic minerals [15].

Chemical compositions of both flowback and produced water has been extensively investigated in several papers and reports. Chemical composition and concentration of chemical species were measured for flowback and produced water for different formations such as the Marcellus shale formation [14-21], Barnett [19,21], Woodford [22], and Horn River [23]. Also, the United States Geological Survey National Produced Waters Geochemical Database includes the compositions of produced water samples gathered from different formations [24]. Additionally, some studies inspected temporal changes of flowback water composition and concentration of major species. Figure 1.2 shows the changes in chlorine and sodium for two representative flowback water samples from the Western and Eastern United States [25]. These samples were gathered within 30 days following the hydraulic fracturing of wells. The results from this study and other similar studies [15,26] suggest that the concentration of the non-organic compounds in flowback water increases as time goes on. As the production of a fracked well continues most of the water that was initially used in the fracturing fluid returns to the surface within the first weeks of the fracturing process. Therefore, the volume of water derived from the fracturing fluid gradually decreases. Subsequently the concentration of mineral compound in the water returning to the

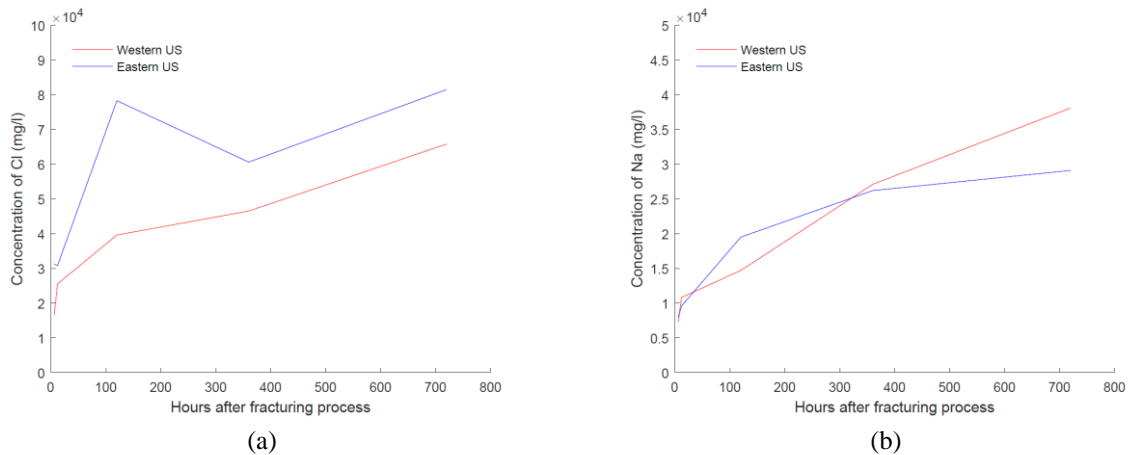


Figure 1.2. Concentration of (a) Cl and (b) Na for Eastern and Western US flowback water samples in terms of hours after fracturing operation [22].

surface increases.

2 Chemical compound of a representative produced water solution

2.1 Methodology

To investigate the effect of produced water on particle emissions from flares a representative solution for produced water needs to be found. Most research papers related to produced water are only focused on the chemical composition of produced water from a specific geographical region. Therefore, it was decided to use a data source with extensive data on produced water from different geographical regions. The United States Geological Survey National Produced Waters Geochemical Database v2.1 provides information on the composition of produced waters sampled from all regions of the United States. This database has information on 161,915 produced water samples and it contains information such as location of the well, date the sample was analyzed, formation type, and chemical species of the produced waters, etc. This database is a collection of 25 individual databases, reports or publications [24]. According to the USGS database “the water samples are commonly collected when a well has production problems or during the initial development of a well” [24]. Based on their explanation it can be inferred that most of the samples from hydraulically fractured wells could be flowback water rather than produced water. It should also be noted that the USGS data base has a great deal of information on numerous elements (predominately cations and anions) of produced waters, however, some chemical compounds existing in produced water samples, such as compounds used in fracturing fluid, are not included in the USGS database. In order to apply data analysis on this database a MATLAB code was used.

2.1.1 Categorization of Produced Water Samples

The USGS database has several well categories. Conventional hydrocarbon wells and unconventional well types were included. Based on the objective of this project the following well types were investigated:

- Conventional hydrocarbons: Gas and oil that are extracted by the natural pressure of the wells or compression operation, after the drilling process is complete.
- Shale gas: Natural gas which is trapped tightly in a shale formation [27].
- Tight gas: Natural gas extracted from low permeability reservoir rocks (less than $10^2 \mu\text{m}^2$) and low porosity (less than 10%) [28], where the rock formations are typically sandstones or sometimes limestones.
- Tight oil: Oil that is contained in carbonate rocks and tight sandstone interbedded in the vicinity of source rocks¹ [28].

The MATLAB code was used to filter the samples based on the type of wells mentioned. The date of samples in the USGS database is quite extensive and it ranges from 1930 to 2014. However,

¹ Rocks that have the capability to produce hydrocarbons or have produced hydrocarbons

since the use of horizontal drilling and hydraulic fracturing has been increasingly used in the past two decades [29] it was decided to only include samples since 1990.

2.1.2 Prominent species in the produced water samples

After categorizing the samples of USGS based on the well type and date, chemical species analysis was conducted to determine which species are common in all of these categories and which species are measured exclusively in each category. Also for each species the median concentration was determined. The main reason that in the statistical calculation median is used instead of mean is that the concentrations vary by orders of magnitudes, therefore, the mean is highly influenced by the samples with high concentrations. Due to this the mean is not a representative of a frequently occurring sample. The results of the species measured in all well types and species measured only in unconventional wells are shown in Tables 2.1 and 2.2.

Table 2.1. Median concentration (mg/L) of species measured in both conventional and unconventional produced water samples

	Ba	Br	HCO ₃	Ca	Cl	Fe _{tot}	K	Li	Mg	Na	SO ₄	Sr87-86	Sr
CONV	3.17	13.8	281	10423.5	173590.5	5	2290	14.35	1215	85500	966	0.71	53.8
SG	5.0	308.0	1211.5	119.2	6963.6	4949.4	202.0	37.8	19.0	5881.0	167.0	0.7	744.5
TG	11.1	46.1	1213.0	46.0	3798.0	13.0	34.0	1.0	8.0	2720.0	25.0	0.7	3.4
TO	60.8	693.0	624.6	7063.4	74923.9	40986.1	4314.1	43.6	984.2	55485.4	1891.8	0.6	1088.8

CONV: conventional wells, SG: shale gas, TG: tight gas, TO: tight oil

Table 2.2. Median concentration (mg/L) of species only measured in unconventional produced water samples

	NO ₂	NO ₃ NO ₂	NH ₄	PO ₄	S	SO ₃	Sn	Ti	Tl	C ₂ H ₆ O ₂	C ₃ H ₆ O	C ₇ H ₈	C ₈ H _{10_XY}	C ₈ H _{10_ETH}	H ₂ S	CO ₂	OH
SG	3.0	0.3	67.1	0.2	3.0	12.0	1.0	0.3	0.1	31.0	90.4	1.6	114.0	8.9	2.0	264.0	88.0
TG	–	–	–	–	–	–	–	–	–	–	–	–	–	–	2.1	264.0	0.4
TO	–	–	–	–	–	–	–	–	–	–	–	–	–	–	2.1	343.6	–

SG: shale gas, TG: tight gas, TO: tight oil

A secondary purpose of this investigation is to determine “typical” concentrations of important substances which will be used to make a synthetic produced water solution for future experiments as part of the FlareNet project. Based on the number of samples and the median concentration of species, the most prominent chemical species were selected to be included in the final synthetic produced water solution. These species are Cl, Na, Ca, K, Mg, HCO₃ and SO₄. The selected species were also included in other chemical analyses of produced water and flowback water in other research [14-21].

2.1.3 Dataset Generation Based on Regions and Formations

By further analysis of the datasets obtained after applying the preceding filters (date and well types) it was concluded that the unconventional samples are from specific geographical regions or geological formations. All of the samples from unconventional databases were from Bakken, Woodford and Wyoming regions; with Bakken mostly consisting of tight oil, Woodford consisting of tight gas and shale gas and Wyoming consisting of tight gas. On the other hand, since the

selected regions are from different parts of the United States the geological formation and rock chemical compositions could be quite different. Therefore, the unconventional well types were categorized based on the above regions and formations. The regional categorization was only applied to unconventional well types. Finally, four datasets (Conventional hydrocarbons, Bakken, Woodford, Wyoming) were obtained and further chemical analyses were conducted on these four datasets.

2.2 Results

The MATLAB code was used to produce probability density functions² for the concentration of each prominent chemical species in each dataset. It is worth mentioning that in addition to the three categories of unconventional wells (Bakken, Woodford, Wyoming), the probability density functions for the overall unconventional samples are also shown. The results of these probability density functions are shown in Figures 2.1-2.7.

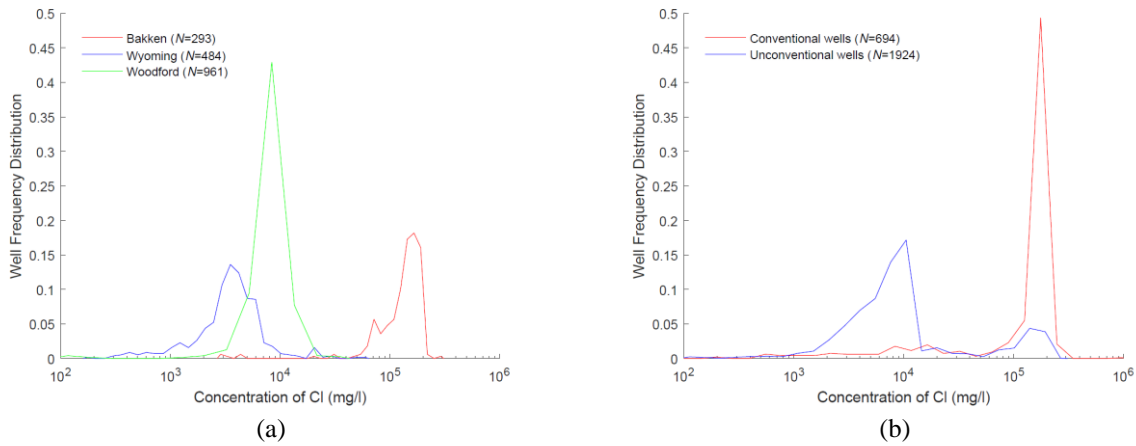
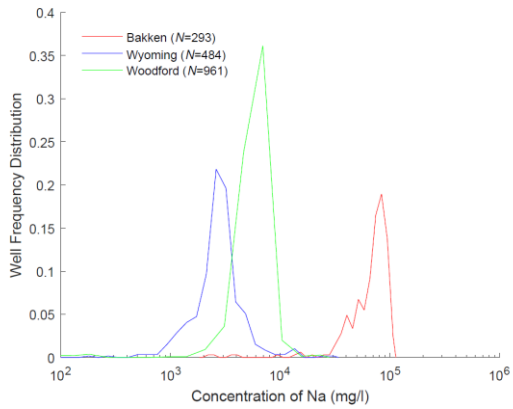
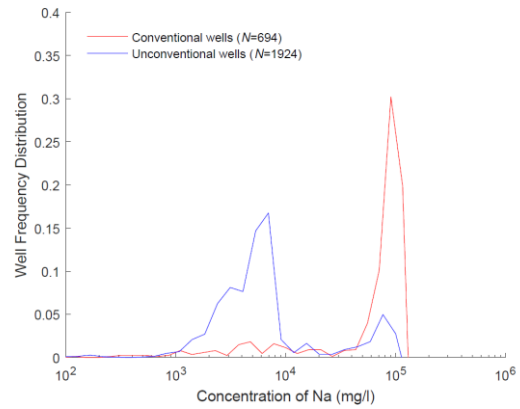


Figure 2.1. Probability density functions of Cl concentration for (a) unconventional wells and (b) all conventional and unconventional wells.

² The parameter used in the y axis of the graphs is $dF/d \log(c_{i+1}/c_i)$ and is the normalized frequency function in logarithmic scale.

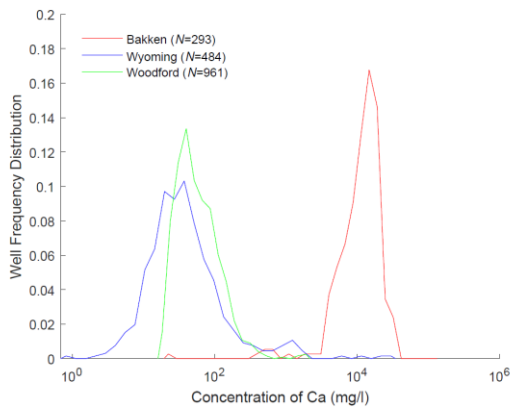


(a)

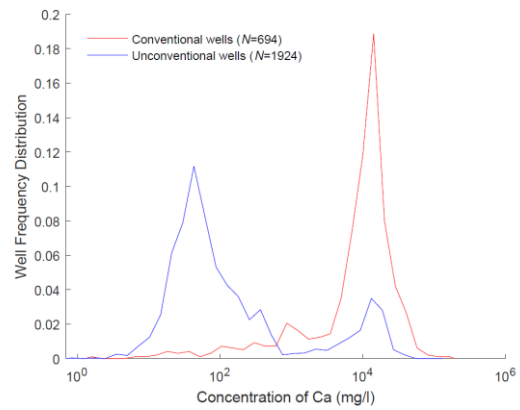


(b)

Figure 2.2. Probability density functions of Na concentration for (a) unconventional wells and (b) all conventional and unconventional wells.

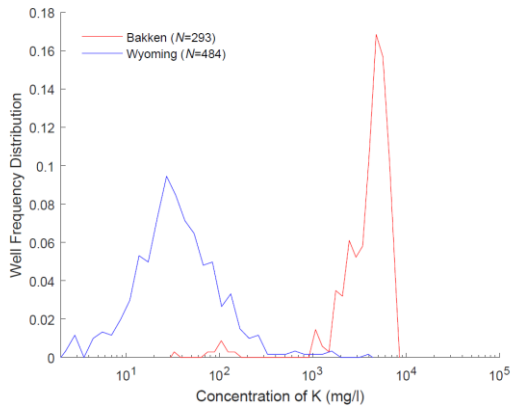


(a)

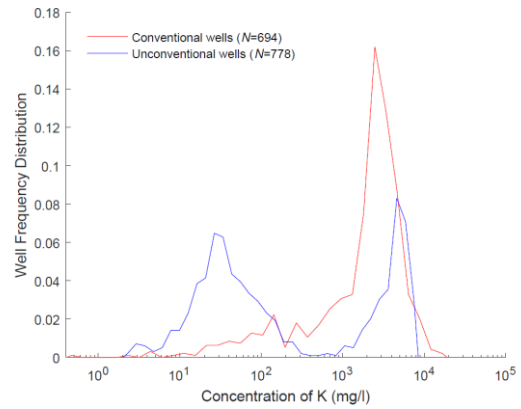


(b)

Figure 2.3. Probability density functions of Ca concentration for (a) unconventional wells and (b) all conventional and unconventional wells.

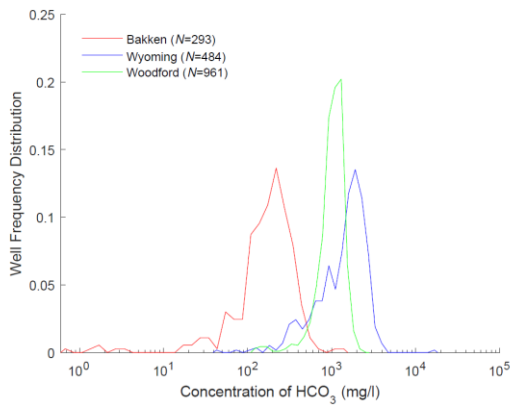


(a)

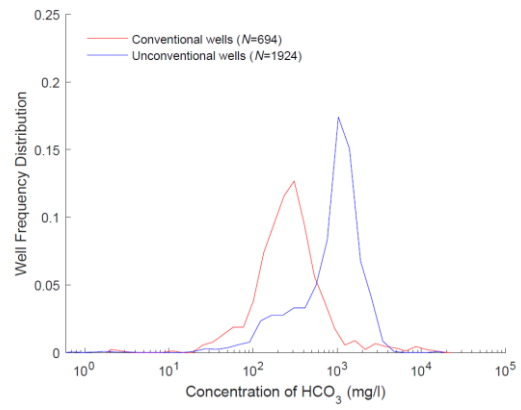


(b)

Figure 2.4. Probability density functions of K concentration for (a) unconventional wells and (b) all conventional and unconventional wells. (Note: No data was available for Woodford).



(a)



(b)

Figure 2.5. Probability density functions of HCO_3 concentration for (a) unconventional wells and (b) all conventional and unconventional wells.

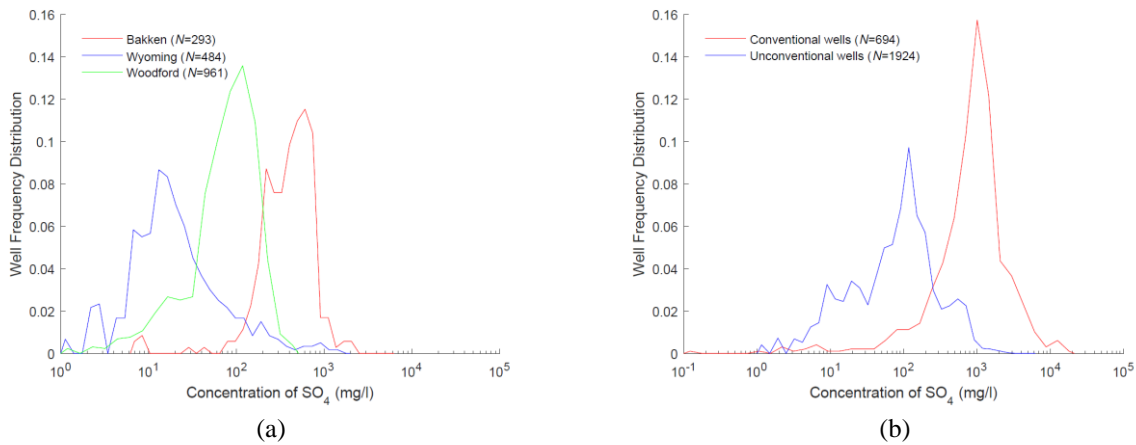


Figure 2.6. Probability density functions of SO_4 concentration for (a) unconventional wells and (b) all conventional and unconventional wells.

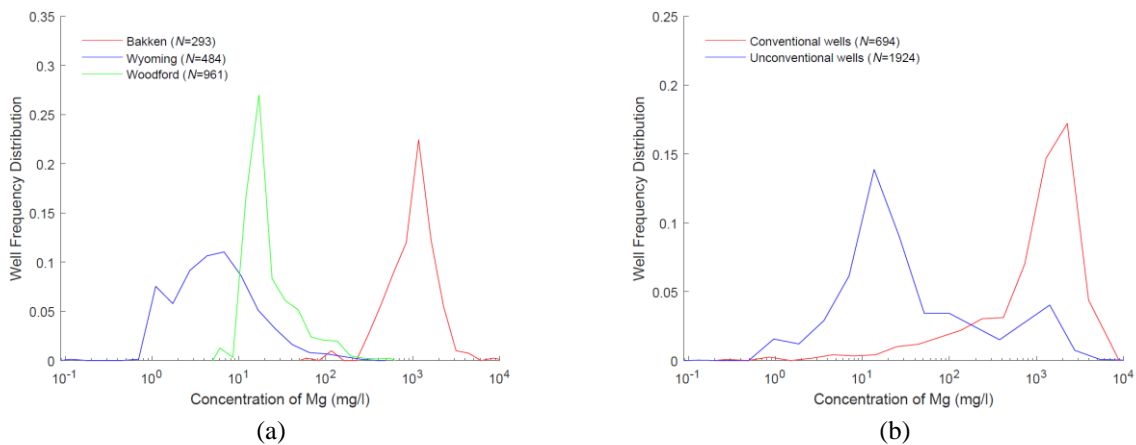


Figure 2.7. Probability density functions of Mg concentration for (a) unconventional wells and (b) all conventional and unconventional wells.

For each species in each dataset the median was determined. Table 2.3 shows the medians of each species in each dataset.

Table 2.3. Median concentration (mg/L) of species from selected regions and formations.

Regions and formations	Median concentration (mg/L) based on species						
	Cl	Na	Ca	HCO_3	SO_4	K	Mg
Bakken (293 samples)	144989	73400	12698	183	416	4520	1111
Wyoming (484 samples)	3644.5	2745	32	1584.5	17	33	5
Woodford (961 samples)	8500	5774	48	1049	84	–	19
Conventional wells (694 samples)	177613	91200	11254.6	262	972	2340	1368.3

2.3 Discussion

The figures show that the conventional hydrocarbon dataset has the highest median concentration of cations and chlorine. This is likely due to the fact that the produced water from conventional hydrocarbon wells is mostly brine water and it is not diluted with fresh water from the fracturing process. On the other hand, the lowest concentration of cations and chlorine can be found in the Wyoming dataset. Thus, the conventional hydrocarbon dataset can be a representative value of produced water with a high concentration of species, while the results from Wyoming can be treated as a representative value of produced water with low concentration of species.

Comparing these high and low concentration representative with the species concentrations reported in other papers show that the concentration of produced water and flowback water samples measured in other studies are between these two extremes. Table 2.4 compares the concentration of species in conventional wells and Wyoming with average flowback water samples from other regions of the United States. Table 2.5 compares the concentration of species in conventional wells and Wyoming with average produced water samples from four tight oil resource plays in Alberta and Saskatchewan, Canada.

Most of the reported species concentration fall between the two cases of conventional wells and Wyoming; therefore, for future FlareNet work, the synthetic produced water will be based on the concentration of species in those two cases (conventional wells and Wyoming). By applying this assumption, the synthetic produced water must be mixture solution of the salt and acids outlined in Table 2.6.

Table 2.4. Comparison of conventional well samples and Wyoming with results of [19].

Species	Concentration (mg/L)				
	Conventional wells	Wyoming	Fayetteville (AR)	Marcellus (PA)	Barnett (TX)
Cl	177613	3644.5	8042.3	43578.4	23797.5
Na	91200	2745	5362.6	24445	12453
Ca	11254.6	32	256.3	2921	2242
HCO ₃	262	1584.5	1281.4	261.4	289
SO ₄	972	17	149.4	9.1	60
K	2340	33	–	–	–
Mg	1368.3	5	77.3	263.1	253

Table 2.5. Comparison of conventional well samples and Wyoming with results of [30].

Species	Concentration (mg/L)					
	Conventional wells	Wyoming	Cardium	Slave Point	Colorado Group	Waskada/Spearfish
Cl	177613	3644.5	5104	88435	27000	93581
Na	91200	2745	2431	37325	15547	53593
Ca	11254.6	32	934	11793	641	2551
HCO ₃	262	1584.5	1098	164	463	389
SO ₄	972	17	226	969	152	2104
K	2340	33	169	503	208	585
Mg	1368.3	5	143	3053	367	746

Table 2.6. Chemical compound concentrations in the synthetic produced water for both low and high extremes.

Chemical Compound	Concentration (mg/L)	
	Low extreme (Wyoming)	High extreme (conventional wells)
NaCl	5983.9	252621
NaHCO ₃	2181.8	360.8
CaCl ₂	88	30950.15
KCl	62.5	4434.6
MgCl ₂	4	4503.6
MgSO ₄	21	1215.3

3 Small-scale diffusion flame experiment³

Extractive techniques have been extensively used to investigate soot formation in combustion processes. One such technique is probe sampling, which has been employed for soot measurements from flames during the last few decades. This method offers the advantage of extracting samples directly from a known location in the flame and then using standard aerosol instruments to perform the measurement; however, concerns exist whether the measured sample is representative of that in the flow at the sample location due to the presence of the probe in the flow and flame (such as stagnation effects) and remains representative during the handling of the sample in tubing prior to measurement.

Probe sampling was also used extensively to investigate soot formation in premixed flames [31-

³ An unabridged version this chapter has been published as M. Kazemimanesh, A. Moallemi, J.S. Olfert, L.W. Kostiuk (2016). Probe sampling to map and characterize nanoparticles along the axis of a laminar methane jet diffusion flame, Proceedings of the Combustion Institute. (<http://dx.doi.org/10.1016/j.proci.2016.06.169>)

36]. In some of these studies, sampled soot particles were diluted in multiple stages to reach a high overall dilution and then directed to particle measuring instruments [31,33,37,38]. Multi-stage dilution systems have the advantage of decreasing particle concentrations to within the measuring range of particle measurement instruments; however, such systems lack very high immediate dilution of the sample, which could possibly result in changing the particle size distribution if particle concentrations are very high at a sample point in the flame. Zhao et al. [32] pioneered an improvement and characterization of the probe sampling technique and used it extensively to extract soot samples from ethylene premixed flat flames.

The use of probe sampling for investigation and characterization of soot nanoparticle evolution in a gaseous diffusion flame has not been tested. Therefore, the main objective of the study on a small-scale experiment was to improve and characterize probe-sampling techniques for the investigation of the evolution of soot nanoparticles along the centerline of a methane laminar diffusion flame with high spatial resolution. Besides providing new data and insights on soot particle formation and evolution through a laminar methane diffusion flame, this work explores a large dynamic range of dilution ratio immediately after extraction to quantify what is required to maintain the integrity of the sample for measurement.

3.1 Experimental setup

The experimental setup is shown schematically in Figure 3.1 and consists of a co-flow diffusion flame burner, a variable-dilution sampling system, and the nanoparticle measurement and gas analyzer suite.

3.1.1 Co-flow burner

A well-studied co-annular burner described by Santoro et al. [39,40] with 11.1 mm fuel tube and 101.6 mm co-flow air tube was used to produce a stable laminar diffusion flame at atmospheric pressure. For this study, methane was used as the fuel due to its lower sooting tendency compared to heavier hydrocarbons such as ethylene. Fuel and air flow rates in the burner were maintained at 0.35 and 70.0 SLPM (standard liters per minute at 25°C and 1 atm), respectively, by using two mass flow controllers (Cole-Parmer, Model 32907-71, and Omega, Model FMA-774A, respectively). These flow rates resulted in a stable diffusion flame with a visible height of 61 mm. The temperature of the edge of fuel tube was at ~450 K. The centerline flame temperature for a similar burner is ~500–1500 K [41]. To avoid the entrainment of ambient air and to minimize the effect of room air currents, a quartz tube shield with diameter of 115 mm was mounted around the burner and a ceramic honeycomb placed atop of the shield, as mentioned in earlier studies [42]. The burner was mounted on two motor-driven translation stages with an accuracy of 0.03 mm for horizontal movement. Two longitudinal narrow slots in the shield allowed vertical translation of the sampling probe through the flame tip.

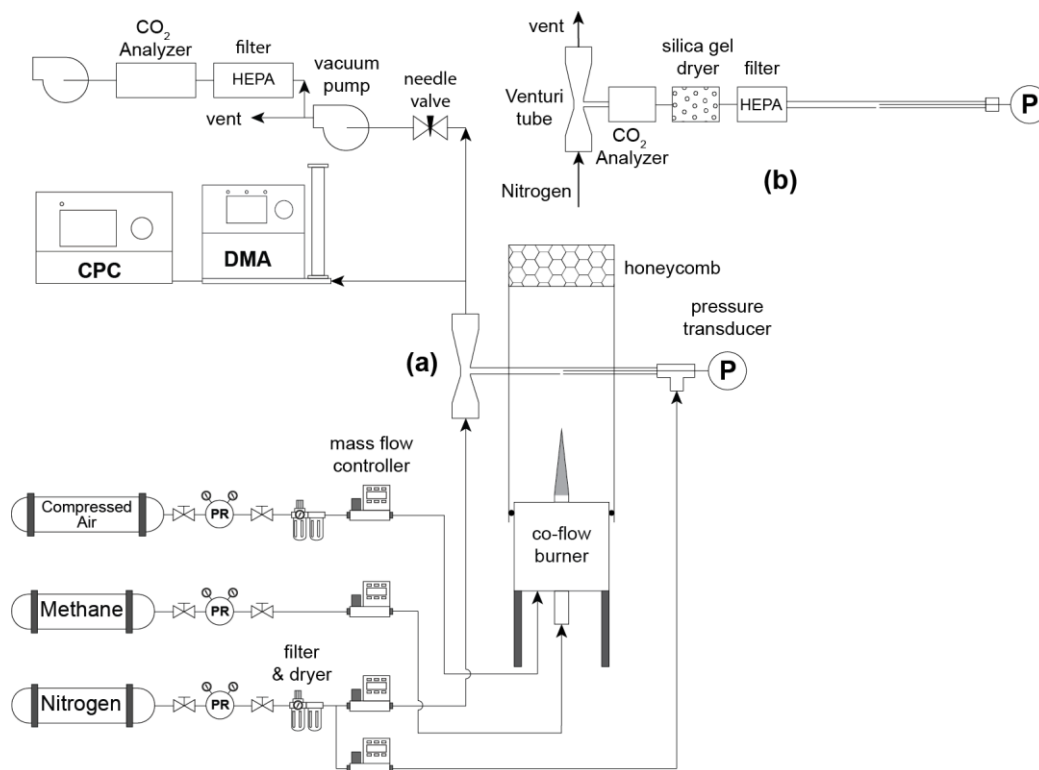


Figure 3.1. Schematic of the experimental setup for (a) diluted sampling, and (b) modified sampling system for undiluted sampling.

3.1.2 Sampling system

The sampling system consisted of a stainless steel tube (3.2 mm OD and 2.16 mm ID) with a 0.5 mm pinhole in the middle that was positioned horizontally above the flame, pinhole facing downward. The sampling system was mounted on a separate motor-driven translational stage with an accuracy of 0.03 mm for movement along the z -axis. The pinhole was centered along the centerline of the burner before each test using the three translation stages by using a device that fits into the throat of fuel tube and has a centrally located needle on which to align the sample port. Pinholes smaller than 0.5 mm resulted in complete clogging of the pinhole in a time less than the duration of a measurement with the particle measurement suite. The 0.5 mm pinhole provided enough time for carrying out particle measurements; however, it needed to be cleaned by a fine wire periodically.

Sampling of particles with a probe, especially when they are at high concentrations, requires high amounts of dilution to immediately quench chemical reactions and avoid particle-particle coagulation. Dilution (on the order of thousands of times) was achieved by flowing particle-free dry nitrogen at a flow rate of 10.0 SLPM at one end of the sampling tube using a mass flow controller (Cole-Parmer, Model 32907-67). For further dilution, the other end of the sampling tube was connected to the throat of an aluminum Venturi tube with inlet and throat diameters of 10 mm and 5 mm, respectively. Clean dry nitrogen at a flow rate of 30.0 SLPM was maintained at the

inlet of the Venturi tube using a separate mass flow controller (Omega, Model FMA-5540). Therefore, the second stage dilution through the Venturi tube was 4:1 based on the flow rates through the inlet and the throat. A needle valve and diaphragm vacuum pump (GAST, Model DAA-P501) connected to the outlet of the Venturi tube established a slight vacuum throughout the dilution system such that flow was into pinhole. A key feature of the sample probe was a 0.8 mm OD stainless steel tube inside the sampling probe, inserted from the upstream side, to measure the gauge pressure at the pinhole. Previous studies [6] measured upstream and downstream pressures in the sampling probe and used calibration of pressure drop as a function of distance to find the pressure at the pinhole location; however, the current method gave a direct reading of ΔP across the pinhole.

3.1.3 Particle measurement suite

Sampled particles were extracted from the main sample flow to the particle measurement suite through a branch at the outlet of the Venturi tube. The size distribution of particles was measured using a scanning mobility particle sizer (SMPS; TSI Inc., Model 3080), which consisted of a nano differential mobility analyzer (nano-DMA; TSI Inc., Model 3085) for particle sizing and a condensation particle counter (CPC; TSI Inc., Model 3776) for particle counting. The aerosol and sheath air flow rates were set at 1.5 L/min and 15 L/min, respectively, for a full-width half-maximum resolution of one tenth the mobility set point and provided a particle sizing range of 2–60 nm. Typically, a particle size distribution was obtained from a 30–40 s scan after an ~10 min warm-up time for flame stabilization. The particles were drawn into the nano-DMA via silicone conductive tubing by the CPC pump.

3.1.4 Dilution ratio measurement

The mole fraction of CO₂ in diluted and undiluted samples was measured online by two non-dispersive infrared CO₂ analyzers (LI-COR, Model LI-840A, and Gas Sensing Solutions, Model COZIR-20%, respectively) to determine the overall dilution ratio. Figure 3.1 shows the setup for both cases. In the diluted case, a ΔP was maintained through the pinhole using the needle valve at a certain height above burner (HAB; height above fuel tube exit plane). The diluted sample was then measured by the SMPS and the low-range CO₂ analyzer. In the undiluted case, the ΔP across the pinhole was set to be the same as the diluted case for a specific HAB by controlling the inlet flow to the Venturi. Assuming the same temperatures irrespective of whether diluted or not at a certain HAB, the volumetric flow rate through the pinhole remained the same in both diluted and undiluted cases for a certain ΔP . In the undiluted case (modified setup shown on top right of Fig. 3.1), the diluting nitrogen flow at one end of the probe was blocked and the sample was drawn through the pinhole using the Venturi tube and measured by a wide-range CO₂ analyzer after being filtered and dried by silica gel.

Assuming similar composition of sample gas in diluted and undiluted cases, the overall dilution ratio (DR) is calculated by

$$DR = \frac{X_{\text{CO}_2, \text{undiluted}@P,T}}{X_{\text{CO}_2, \text{diluted}@P,T}} \quad (1)$$

where $X_{\text{CO}_2, \text{undiluted}}$ and $X_{\text{CO}_2, \text{diluted}}$ are the mole fraction of CO_2 in the undiluted and diluted samples at the same pressure and temperature, respectively. When measuring the size distribution of particles, the ΔP across the pinhole was typically maintained in the range of 30–80 Pa for various heights above burner to achieve overall dilution ratios of 10,000 to 25,000. This low flow rate caused minimal perturbation to the flame. The dilution ratio through the pinhole can be estimated by dividing the overall dilution ratio by the dilution ratio of second stage (i.e., 4). Therefore, an immediate dilution ratio of up to ~6,000 was achieved at the pinhole location. This immediate dilution with nitrogen at ~300 K also ensured quenching of chemical reactions inside the probe. As mentioned in the introduction, some studies [31,33,37] have achieved high overall dilution ratios by combining several low-dilution stages, which could possibly lead to coagulation of particles and change their size distribution.

Considering a typical $DR=20,000$ and dilution ratio of 5,000 through the pinhole, the sample flow velocity through the clean pinhole was ~74–85 cm/s resulting in a residence time of ~0.6–0.7 ms. The residence time for particles in the sampling probe from the pinhole to the throat of Venturi tube was ~2.2 ms. The maximum concentration of nanoparticles measured in the same section of the probe after dilution through the pinhole was $\sim 26 \times 10^7 \text{ cm}^{-3}$. The corresponding coagulation coefficient for this concentration of particles is equal to $\sim 14.9 \times 10^{-10} \text{ cm}^3/\text{s}$ using the method described in [43], and the percentage of particles undergoing coagulation in the probe was always below 0.08%. After entering the Venturi tube, nanoparticles were diluted further to a maximum concentration of $\sim 6.5 \times 10^7 \text{ cm}^{-3}$, ensuring that coagulation of particles was less than ~4.7% for a residence time of ~0.51 s during transport to the SMPS.

3.2 Results and discussion

3.2.1 Effect of dilution on particle size distribution

A wide range of dilution ratios were used at each height above burner to investigate its effect on the measured particle size distribution (PSD). Particle losses or particle-particle coagulation can change the particle size distribution. For low dilution ratios, where coagulation is significant, it is expected to measure larger particles with reduced number concentration. Once a critical dilution ratio is reached or the particle number concentration is sufficiently low, the effect of coagulation is negligible and the measured particle size and concentration becomes independent from the dilution ratio. Zhao et al. [32] and Camacho et al. [36] refined this probe sampling technique to achieve this criterion for premixed flames and we followed the same path to obtain the critical dilution ratio for the current diffusion flame. Figure 3.2 shows the variations of particle size distribution for an HAB=36 mm when the dilution ratio was changed by more than an order of magnitude from 1,150 to 20,700. The total number concentration of particles was obtained from $N = DR \cdot N_{\text{SMPS}}$, where N_{SMPS} is the particle number concentration measured by SMPS. With low

dilution ratio, the PSD was unimodal and no particles smaller than 4 nm were detected. As the dilution ratio was increased, the PSD started to become bimodal with a very large number of nanoparticles smaller than 2 nm (only a small fraction of the tail of the first mode in the range of 2–3 nm could be detected by the nano-DMA).

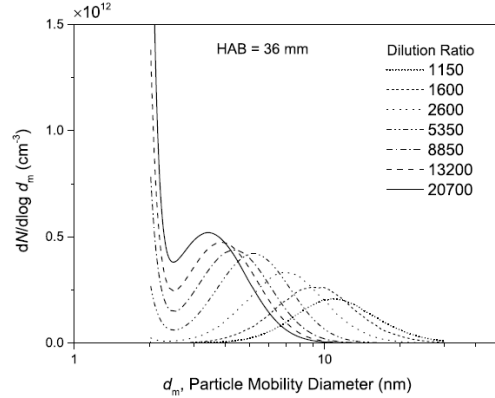


Figure 3.2. Variation of particle size distribution as a function of dilution ratio for HAB=36 mm.

Figure 3.3 shows the change in the particle median diameter of the second mode by variation in dilution ratio. This median diameter was calculated based on a bimodal lognormal fit of the measured PSD. Once the dilution ratio reached the critical value of ~9,000 for this specific HAB, the particle median diameter remained approximately constant. This is consistent with the findings of Zhao et al. [32] and Camacho et al. [36] for premixed flames. In the subsequent sections, only data obtained beyond the critical dilution ratio are presented.

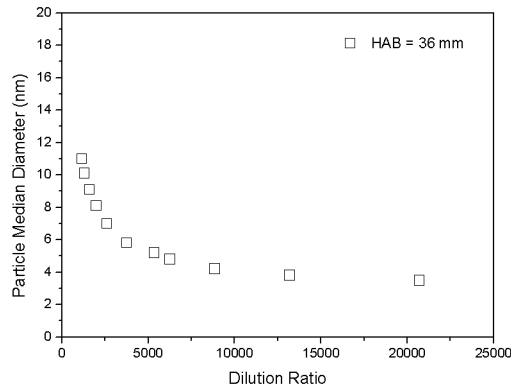


Figure 3.3. Variation of particle median diameter as a function of dilution ratio for HAB=36mm.

3.2.2 Effect of pinhole clogging on particle size distribution

One of the practical drawbacks of sampling particles with a probe, is the clogging of the pinhole over time. Deposition and accumulation of soot particles on the wall of the pinhole as well as on the outer surface of the sampling tube in the vicinity of the pinhole caused gradual clogging of the pinhole reducing its effective diameter. Clogging typically continued until the pinhole was completely blocked and no CO₂ was measured by the analyzer. During clogging, online CO₂ measurements showed that CO₂ mole fraction decreased with time, an indication that sample flow rate through the pinhole was reduced. Moreover, online ΔP measurements revealed that, during

clogging, slightly higher vacuum was measured inside the sampling probe due to partial blockage of the pinhole. The gradual decrease of CO₂ mole fraction showed that from the opposing effects of effective pinhole diameter and ΔP across the pinhole, the former had a greater effect on the sample flow rate through pinhole.

Figure 3.4 shows the effect of clogging on the measured particle size distribution for HAB=41 mm. We noted earlier that dilution ratio affected the PSD considerably. To isolate the effect of dilution ratio, particle size distribution was measured at a specific ΔP (i.e., dilution ratio) while the pinhole was lightly, moderately, or heavily clogged. The required time for complete blockage of the pinhole in this set of tests was ~300 s. The amount of clogging is indicated by the time after the clean pinhole was positioned in the flame and the SMPS scan started. It is clear that the amount of clogging did not have a considerable effect on the particle size distribution. This fact provided ample time for fine adjustment of ΔP (~60–120 s) and measuring PSD as long as the pinhole was not completely clogged. Figure 3.4 also confirms that once a certain dilution ratio was maintained in the dilution system, highly reproducible particle size distributions could be obtained regardless of time or degree of pinhole clogging.

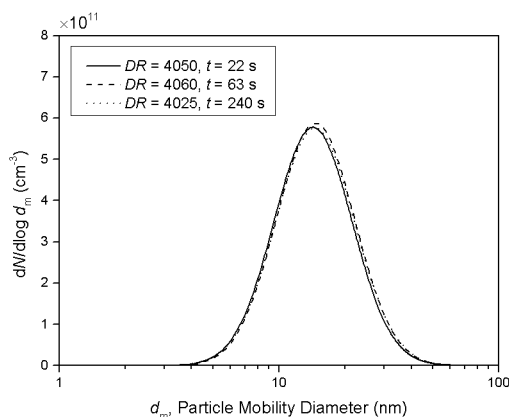


Figure 3.4. Effect of pinhole clogging on particle size distribution for HAB=41 mm. t is the time after the clean pinhole was positioned in the flame and the SMPS scan started.

3.2.3 Evolution of particle size distribution in the flame

Particle size distributions for different heights above the burner along the centerline of the flame were obtained. The purpose of this part of the experiment was to create a detailed map of nanoparticles along the central axis of the laminar diffusion flame and to investigate particle evolution along the centerline of the flame.

Figures 3.5-3.7 show the particle size distribution for HAB from 30 mm to 62 mm. For the sake of clarity, the particle size distributions are broken into three plots to better represent the trends in particle evolution. Below HAB=30 mm, the SMPS could not detect any particles. At the onset of particle nucleation at the height of 30 mm, a small fraction of the tail of the PSD could be detected which mostly consisted of nanoparticles smaller than 2 nm. At 35 mm, the PSD became bimodal, with a larger diameter mode. Like before, only a fraction of the tail of the first mode could be detected which consisted of particles smaller than 3 nm; however, the number of particles in this

mode was much more than that of the second mode. At higher heights above burner until 38 mm, the second mode increases in both diameter and number as the first mode gradually disappears. By fitting the bimodal PSDs with two lognormal distributions, the median diameter of the second mode is estimated to change from ~ 3 nm to ~ 6 nm when the HAB was changed from 35 mm to 38 mm. The PSDs show particle nucleation at lower heights and the coagulation of these nucleated nanoparticles at higher heights to form larger particles with reduced number concentration.

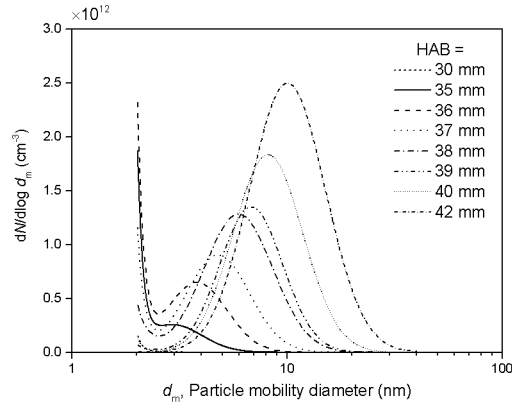


Figure 3.5. Particle size distributions for HAB=30–42 mm.

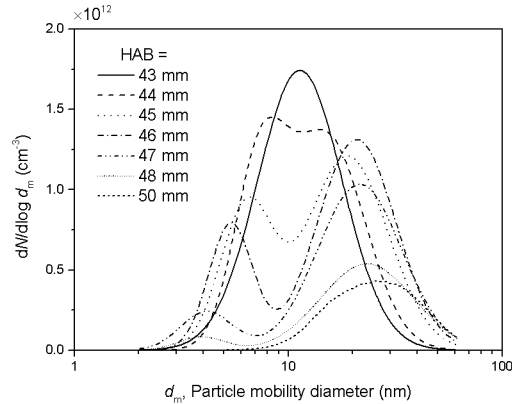


Figure 3.6. Particle size distribution for HAB=43–50 mm.

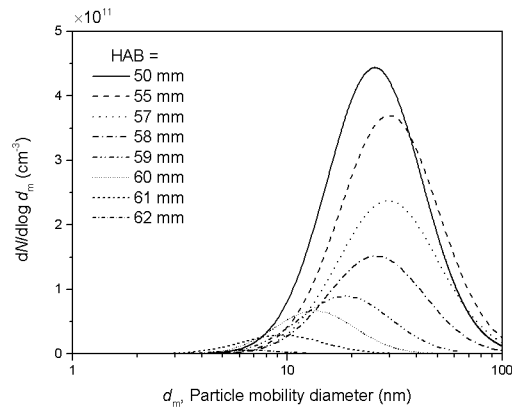


Figure 3.7. Particle size distribution for HAB=50–62 mm.

At heights of 39 to 42 mm, the PSD was mostly unimodal with both its median diameter and

number concentration growing as HAB increased. The particle median diameter grew to ~10 nm for the height of 42 mm. Closer investigation of these PSDs revealed that they included the tail of the small first mode, which decreases with height above the burner. It should be noted that the geometric standard deviation, σ , of the PSD from the heights of 39 to 42 mm varies from 1.44 to 1.50, which is larger than $\sigma = 1.44$ for a self-preserving distribution in the free-molecular regime [44]. Zhao et al. [32] have argued this is indicative of particle growth not only by coagulation, but also by particle mass growth by surface reaction [45].

From the height of 42 mm to 43 mm, the particles growth continued from 10 nm to 11.3 nm (median size) while their number concentration decreased. At HAB=44 to 48 mm, the unimodal PSD became bimodal again. We call the left-most mode as Mode I and the right-most mode as Mode II. With increasing height in this region of the flame, the median particle size in Mode II grew larger in diameter from 15 nm to 23.3 nm, while the particles became smaller in diameter in Mode I, and both Modes I and II decrease in number concentration. At the height of 50 mm, Mode I vanished and only Mode II survived. This is an interesting evolution for the particles, which to the knowledge of authors, has not been reported before for diffusion flames in the literature and needs further investigation to explain the transformation of unimodal to bimodal PSD and back again. Presumably, the particles in Mode I and Mode II continue to coagulate and form larger particles in Mode II in smaller numbers. It is speculated that particles in Mode I experience oxidation between the heights of 44 to 48 mm as both their median diameter and number concentration became smaller in this region. If this is the case, then particle coagulation and oxidation regions overlap at these heights.

At the heights of 50 mm to 55 mm, the PSD was unimodal and the median particles continued to grow to ~30 nm and their number concentration ~decreased probably due to coagulation. From the height of 57 mm to the tip of the flame (61 mm), the median particle diameter sharply decreased from ~30 nm to ~9 nm while its number concentration dropped significantly, presumably due to particle oxidation. At HAB=62 mm, just outside the tip of the flame, the particles continued to shrink in size and their number concentration was greatly reduced.

3.3 Conclusions

Nanoparticles generated by combustion of methane in a laminar jet diffusion flame were characterized systematically by direct sampling through the pinhole of a probe and sizing them with a nano-DMA. Particular attention was paid to verify the validity of probe-sampling technique in measuring nanoparticles from highly reacting flows. A method for the measurement of dilution ratio was introduced by measuring CO₂ concentration continuously during the tests for diluted and undiluted samples, which could substitute other methods of determining dilution ratio based on computation or offline measurement of CO₂ concentration. Analytical and experimental results showed that particle-particle coagulation, which is a challenge for particle size distribution measurement, was negligible in this study. The effect of dilution ratio on the shape of the particle size distributions was characterized, confirming that particle size distributions became independent from the dilution ratio when using very high and immediate dilution. Moreover, it

was shown that the degree of clogging of the pinhole had no considerable effect on the particle size distribution.

Size distributions of particles larger than 2 nm were obtained for various heights above burner, covering early nucleation and growth to oxidation regions. It was found that the PSD in the nucleation region was bimodal and gradually turned into a unimodal PSD due to particle growth. At the height of 44 mm above the burner, the PSD started to become bimodal again with the second mode growing in diameter and the first mode gradually decreasing in size until it vanished. It is speculated that particles in the first mode experienced oxidation while the second mode represented continuation of particle coagulation up to a median of 30 nm in diameter. At the height of 57 mm, particles started to oxidize gradually until the tip of the flame where they reached a median diameter of 9 nm and in very low concentrations.

4 Lab-scale turbulent flame experiment⁴

As discussed in Section 1, among the measured constituents, sodium cations (Na^+) and chlorine anions (Cl^-) showed significant increases in concentration when comparing injected fracturing fluid composition to flowback water recovered at various times after injection. Na^+ increased over 140x its total injected concentration of ~125 mg/L in six hours and over 520x by day 30. Similarly, Cl^- increased 76x and 400x its initial injected concentration of ~95 mg/L in six hours and 30 days, respectively [46]. Volume recovery relative to injected volume at various well locations can be as low as 10% or as high as 80% [4,11,48], likely depending on well-type (vertical or horizontal), formation geology, and depth of well. It is possible that fracking fluids mix with formation water (water found at the gas or oil source) [49], causing increased levels of salts to be seen in flowback fluids. Formation water can have a total dissolved solids (TDS) content similar to that of sea water (35,000 mg/L) to over 400,000 mg/L [49].

As mentioned in Section 1.1, droplets below the AER size restriction (300 μm) have the potential to enter the flare stream [12]. Effects and emissions due to chlorinated species and NaCl in combustion environments are well-researched in specific combustion contexts (e.g., chlorinated coals [50-52], biofuels [53-55], chlorinated hydrocarbons [56-59], entrained chloroform in acetylene [60], and extinction studies [61,62]). The objectives of the lab-scale experiment were to determine effects on flare emissions and performance in a model setting by injecting salt water (aqueous NaCl) and hydrochloric acid at known concentrations and flow rates in the form of droplets smaller than the AER allowable limits, into the exit plane of a lab-scale turbulent flame. Combustion products were measured and analyzed with the intent of determining liquid loadings and concentrations needed to have a perceptible effect on flame behaviour.

⁴ An unabridged version of this section is published as A.M. Jefferson, D.J. Corbin, M.R. Johnson, A. Vali, L.W. Kostiuk (2015). Experimental Examination of Injected Salt Water and Hydrochloric Acid Solutions on the Carbon Conversion and Emissions of Turbulent Non-Premixed Flames, Proceedings of Combustion Institute–Canadian Section, Spring Technical Meeting, University of Saskatchewan, May 11-14.

4.1 Methodology

Experiments were performed in Carleton University's lab-scale flare facility illustrated by Figure 4.1(a). A specialized burner and droplet injection system designed in collaboration with the University of Alberta allowed for controlled injection of liquid droplets into the flare gas stream. Gas bottles of high-purity hydrocarbons were used to create a fuel gas mixture of desired composition and flow rate controlled through species-dedicated mass flow controllers. The fuel gas was directed to a burner placed in a 1.7 m deep pit. Emissions were captured with excess dilution air by a large overhead ventilation hood. Two concentric (1.5 and 3 m diameter) settling screens were installed to eliminate any flow disturbances around the flame that could be caused by air flows in the open lab or from air supplied from perforated tubing around the outer bottom edge of the pit. Gaseous- and solid- phase (soot) species were measured with an MKS 2030 Fourier Transform Infrared (FTIR) spectrometer and Artium LII200 Laser Induced Incandescence (LII) instrument, respectively. Detection limits for measured species were: 0.15 ppm_v for carbon monoxide (CO), 0.1 ppm_v for methane (CH₄), 0.5 ppm_v for nitric oxide (NO), 0.05 ppm_v for nitrogen dioxide (NO₂), 2% of reading for carbon dioxide, and 20% of the soot volume fraction measured. Species yields and combustion completion were determined using methodologies developed in [31].

The custom atomizing burner seen in Figure 4.1(b) has a 102 mm (4 in) diameter and 51 mm (2 in) outlet nozzle. Within a closed vessel the desired liquid was pressured to 14 kPa (2 psig) with compressed air and displaced to a dual rotameter setup (one each for low and high flows). The weight of the vessel was continuously measured on a scale (0.1 g precision) to confirm the flow rate. The atomizing surface height (see inset of Figure 4.1(b)) was adjustable and set in the burner exit plane. Droplets of 38 μm were delivered to the flare gas stream by the ultrasonic atomizer (Sono-Tek Corp, model number 06-04062) vibrating at 20-48 kHz and were independent of liquid flow rate.

Experiments were completed for a single fuel gas flow rate of 109.45 SLPM, comprised of 88.18%_v methane (CH₄), 8.08%_v propane (C₃H₈), and 3.74%_v butane (C₄H₁₀). Salt water solutions of 5 and 9.1%_m, hydrochloric acid (HCl) solution at 3.15%_m, and deionized (distilled) water were injected at liquid loadings of approximately 5, 10, 20, and 30%_m of flare gas. Note that the mass percentage of chlorine in the 5%_m salt solution is matched in the 3.15%_m HCl solution. A base case of no liquid injection was also completed.

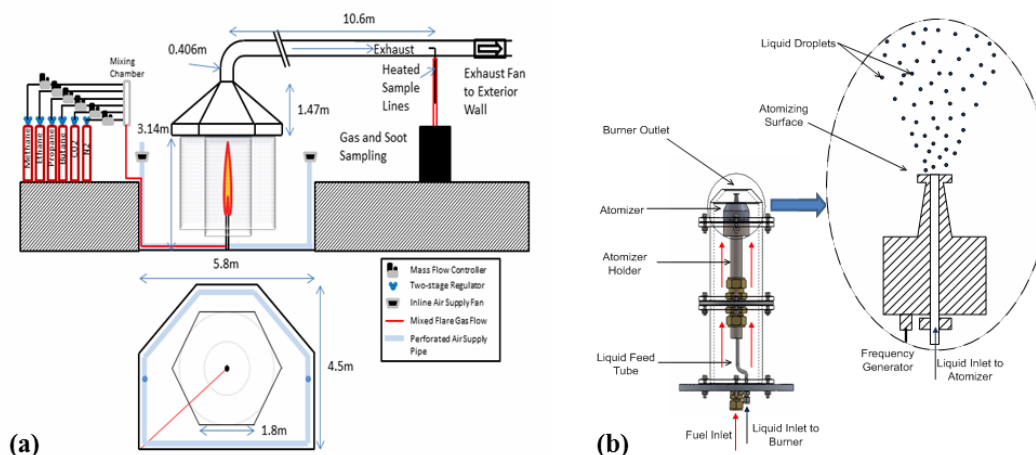


Figure 4.1. (a) Carleton University Lab-Scale Flare Facility; (b) burner and atomizing system

4.2 Results

Increased liquid loading of distilled water over the range tested caused a modest decrease in NO_x (the sum of NO and NO_2) and profound decrease in soot emissions as illustrated in Figure 4.2(a-b). This trend has been seen in studies related to steam-assist flares and other combustion systems [64,65]. CO yield does not appear to be affected by the injection of distilled water (Figure 4.2(c)). The US EPA recognizes that though steam-assist is used to reduce sooting flares, the combustion efficiency (CE) could be negatively impacted, though Figure 4.2(d) shows a slight increase in CE [64-66].

Hydrochloric acid at 3.15%_m solution showed results nearly identical to distilled water for all measured species (CO , CH_4 , NO_x , and soot). The effect on NO_x emissions with the addition of HCl is not well understood though studies primarily show decreasing NO_x with increasing concentrations of HCl gas added to solid fuel reactors [50-52]. Chlorine is believed to significantly affect CO (and subsequently CE) by reacting with radicals used to oxidize CO into CO_2 (e.g., OH , HO_2 , H , OH) [50-52,67]. Results in [50] and its sources experimentally and computationally showed that the hydroxyl radical reaction competition is perhaps the most vital in inhibiting CO oxidation. The two competing reactions are:



Reaction rates calculated using the modified Arrhenius equation, $k(T) = AT^b \exp(-E_A/RT)$, with coefficients from [50,67,68], show that from temperatures of 2000 K, hydroxyls (OH) are consumed approximately 6-7x faster by reaction (3) than reaction (2). Results in [18-20] did not use water/HCl solutions as in the experiments presented here, rather HCl gas in N_2 added to the fluidizing gases for solid fuel reactors from 0 to approximately 5000 ppm. One could then infer that emissions of NO_x , CO , CH_4 and soot could be dominated by effects of water rather than that of chlorine at 3.15%_m. Injection of varying concentrations of HCl would need to be tested to fully comprehend the water-chlorine- CO oxidation mechanisms at play.

Figure 4.2(c) shows an interesting find of this study: CO yield increases with an increase in loading for both concentrations of salt solution, but begins to decrease at approximately 20%_m solution loading. The aforementioned reasoning predicted an increase in CO due to chlorine's inhibiting effects on CO oxidation. A saturation point of this mechanism could be reached at 20%_m loading. However, this would result in an asymptotic rather than a decreasing trend. Methane yields showed similar trends in yield, peaking at 20%_m loading. Similarly intriguing, soot yields for both salt solutions peak at 5%_m loading, rather than 20%_m. The peak soot yield is higher with the stronger salt solution. Though the LII should be insensitive to all particles except soot, it should be noted that results could be affected by sodium ions thus resulting in trends not found previously in literature.

Salt solution injections show more distinct downward trends in NO_x and soot yield than distilled water, though the concentration appears to have minimal effect. The injected water does act as a cooling mechanism thus impeding the formation of NO_x. Dissolving a solute in water lowers the solution's vapour pressure resulting in a higher rate of evaporative cooling in the flame and thus further prohibits NO_x formation. This could explain the differences in salt water to distilled water, yet increasing salt concentration by a factor of ~2 should further accelerate the cooling. Flame suppressant studies show that NaCl/water droplets are a more effective flame suppressant than distilled water alone [61,62], the effects of which could include an increase in incomplete combustion products (e.g., soot and CO) while reducing NO_x.

It is clear from Figure 4.2(c) and (d) that CE is sensitive to CO yields. CE is also affected by soot yield, but as yields of soot are an order of magnitude lower than CO, any response by CE would be dwarfed by changes in CO.

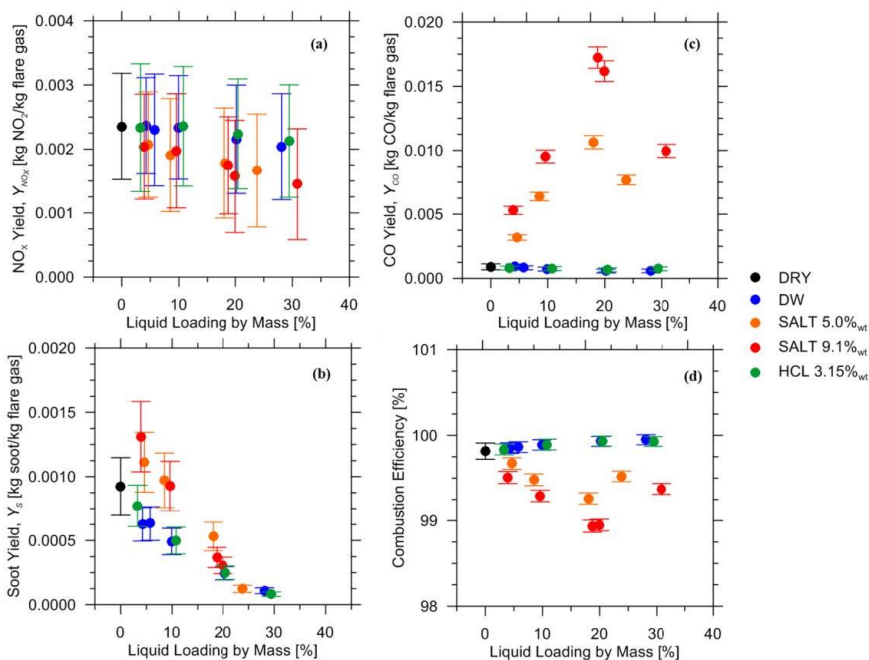


Figure 4.2. Plots of species yields with liquid loading of distilled water, salt water, and HCl solutions. (a) NO_x, (b) Soot, (c) CO, and (d) CE.

4.3 Conclusions

A single fuel gas mixture (88.18% methane, 8.08% propane, and 3.74% butane) at a flow rate of 109.45 SLPM was combusted with and without the injected 38 μm liquid aerosols of distilled water, 5%_m NaCl, 9.1%_m NaCl, and 3.15%_m HCl solutions in water at flow rates as high as 30%_m of the fuel gas. Results show an initial increase in soot and CO yields, though soot peaks at 5%_m liquid loading and subsequently drops to match results seen in distilled water cases, while CO peaks at 20%_m liquid loading. NO_x emissions continuously decrease with increased loading, with salt solutions exacerbating this trend. Potentially contrary to current literature, HCl solutions showed minimal difference from distilled water cases at all liquid loading. Future work is necessary to develop a clear understanding of mechanisms between CO, NO_x, Cl, and soot to explain the trends seen in this experiment. Injection of higher concentrations of HCl and a refined test matrix could indeed provide data needed to draw improved conclusions.

5 Recommendations and Applications

As discussed in Section 1, cation and anion concentrations in the flowback water generally falls between the low extreme case of Wyoming and high extreme case of conventional wells. This shows that fracturing operation can have a significant effect on diluting the flowback water. Future experiments should be focused on injecting droplets of high and low concentration solutions representative of flowback water in both cases of small-scale diffusion flame and large-scale turbulent flame. This will define the lower and higher limits of the effect of flowback water droplets on the emissions of two different types of flames.

Section 2 discussed the evolution of soot nanoparticles along the centreline of a small-scale diffusion flame as the baseline case. Further particle size distribution measurements with injection of droplets of two representative flowback water solutions in the fuel flow prior to combustion shall be conducted. Moreover, the temperature of the flame along its centreline in both cases of without and with additive droplets must be determined. Measurement of flame temperature is essential to understand the phase change of additive particles inside the flame, as well as the effect of added particles on the local temperature at a specified point inside the flame. Furthermore, transmission electron microscopy (TEM) shall be used to obtain images of nanoparticles inside and downstream of the flame in both the baseline case and the flame with additive particles. By comparing the results of such future experiments between the baseline case and the flame with additive droplets, it is possible to investigate particle evolution inside and downstream of the flame, which will provide insight into possible physical and chemical interactions between soot and additive particles. This future work will be carried out in the NSERC funded Flarenet project (<http://www.flarenet.ca>)

In the lab-scale experiment, future experiments should include additive solutions based on the two representative flowback water solutions found in this study. A wider range of fuel flow rate shall

be also explored to capture the potential effects of Reynolds number and Froude number on emission factors. Moreover, the soot yield and NO_x yield measurements in this report have a relatively high uncertainty, which needs to be improved in future experiments. Furthermore, as the LII is (ideally) insensitive to all particulate matters except black carbon (soot), additional particle measurement techniques, such as elemental carbon/organic carbon filter measurements, shall be used to quantify the emission factor of particles other than soot which could potentially form when additive droplets are injected in the flame.

In conclusion, the small-scale and lab-scale experiments in this study are not an actual representative of real flares. Flow characteristics and gas composition of real flares vary widely. Extensive field measurements in an extensive test matrix need to be conducted to have statistically reliable results. Nonetheless, the small-scale and lab-scale experiments provide an insight into the potential effects of additive droplets found in hydrofracturing and flowback operations on the emission factors of flares. The results from these experiments provide a valuable guideline for the future field measurements.

References

- [1] British Petroleum, BP Statistical Review of World Energy, 2014.
- [2] D.J. Lampe, J.F. Stolz, Current perspectives on unconventional shale gas extraction in the Appalachian Basin., *Journal of Environmental Science and Health. Part A, Toxic/Hazardous Substances & Environmental Engineering*. 50 (2015) 434–46.
- [3] R. McCurdy, Proceedings of the Study: Chemical & Analytical Methods Proceedings of the Technical Workshops for the Hydraulic Fracturing Study: Chemical & Analytical Methods, in: *Hydraulic Fracturing Technical Workshop*, US EPA, Arlington, VA, 2011.
- [4] P.J. Edwards, L.L. Tracy, W.K. Wilson, Gradients in Tank-Stored Hydraulic Fracturing Fluids Following Flowback, Newtown Square, PA, US, 2011.
- [5] U.R.S. Corporation, Water Related Issues Associated with Gas Production in The Marcellus Shale, Fort Washington, PA, US, 2011.
- [6] BC Oil & Gas Commission, Frac Focus Chemical Disclosure Registry, (n.d.). <http://fracfocus.ca/> (accessed February 25, 2012).
- [7] T. Bank, Trace Metal Geochemistry and Mobility in the Marcellus Shale Marcellus Shale Samples, in: *Hydraulic Fracturing Technical Workshop*, US EPA, Arlington, VA, 2011.
- [8] N.P. Coleman, Produced Formation Water Sample y Results from Shale Plays, in: *Hydraulic Fracturing Technical Workshop*, US EPA, Arlington, VA, 2011.
- [9] T. Hayes, Characterization of Marcellus and Barnett Shale Flowback Waters and Technology Development for Water Reuse, in: *Hydraulic Fracturing Technical Workshop*, US EPA, Arlington, VA, 2011.
- [10] D.R. Tyner, M.R. Johnson, Emission Factors for Hydraulically Fractured Gas Wells Derived Using Well- and Battery-level Reported Data for Alberta, Canada, *Environmental Science & Technology*. 48 (2014) 14772–14781.
- [11] C. Rivard, D. Lavoie, R. Lefebvre, S. Séjourné, C. Lamontagne, M. Duchesne, An overview of Canadian shale gas production and environmental concerns, *International Journal of Coal Geology*. 126 (2014) 64–76.
- [12] AER, Directive 060: Upstream Petroleum Insdutry Flaring, Incinerating, and Venting, Alberta Energy Regulator (AER), Calgary, AB, 2014.
- [13] U.S. House of Representatives, Chemicals Used in Hydraulic Fracturing, 2011.
- [14] E. Barbot, N.S. Vidic, K.B. Gregory, R.D. Vidic, Spatial and temporal correlation of water quality parameters of produced waters from Devonian-age shale following hydraulic fracturing, *Environmental Science & Technology*. 47 (2013) 2562-2569.
- [15] L.O. Haluszczak, A.W. Rose, L.R. Kump, Geochemical evaluation of flowback brine from

Marcellus gas wells in Pennsylvania USA, *Appl. Geochem.* 28 (2013) 55-61.

[16] E.C. Chapman, R.C. Capo, B.W. Stewart, C.S. Kirby, R.W. Hammack, K.T. Schroeder, H.M. Edenborn, Geochemical and strontium isotope characterization of produced waters from Marcellus Shale natural gas extraction, *Environmental Science & Technology*. 46 (2012) 3545-3553.

[17] K.B. Gregory, R.D. Vidic, D.A. Dzombak, Water management challenges associated with the production of shale gas by hydraulic fracturing, *Elements*. 7 (2011) 181-186.

[18] T.D. Hayes, B.F. Severin, Characterization of Flowback Waters from the Marcellus and the Barnett Shale Regions, (2012).

[19] Horner, Patrick and Halldorson, Brent and Slutz, James A and others, Shale gas water treatment value chain-a review of technologies, including case studies, (2011).

[20] P.F. Ziemkiewicz, Y.T. He, Evolution of water chemistry during Marcellus Shale gas development: A case study in West Virginia, *Chemosphere*. 134 (2015) 224-231.

[21] S.J. Maguire-Boyle, A.R. Barron, Organic compounds in produced waters from shale gas wells, *Environmental Science: Processes & Impacts*. 16 (2014) 2237-2248.

[22] H.R. Acharya, C. Henderson, H. Matis, H. Kommepalli, B. Moore, H. Wang, Cost effective recovery of low-TDS frac flowback water for re-use, US Department of Energy: Washington, DC. (2011).

[23] J. Paktinat, B.J. O'Neil, M.G. Tulissi, Case studies: impact of high salt tolerant friction reducers on freshwater conversation in Canadian shale fracturing treatments, *Proceedings of the 2011 Canadian Unconventional Resources Conference*. (2011).

[24] M.S. Blondes, K.D. Gans, J.J. Thordsen, M.E. Reidy, B. Thomas, M.A. Engle, Y.K. Kharaka, E.L. Rowan, US Geological Survey National Produced Waters Geochemical Database v2. 1 (PROVISIONAL), (2014).

[25] D. McElreath, Comparison of hydraulic fracturing fluid composition with produced water following fracturing-Implications for fate and transport, 600 (2011).

[26] Zolfaghari Sharak, Ashkan and Noel, Mike and Dehghanpour, Hassan and Bearinger, Doug and others, Understanding the Origin of Flowback Salts: A Laboratory and Field Study, (2014).

[27] R.D. Vidic, S.L. Brantley, J.M. Vandenbossche, D. Yoxtheimer, J.D. Abad, Impact of shale gas development on regional water quality, *Science*. 340 (2013) 1235009.

[28] J. Chengzao, M. Zheng, Y. Zhang, Unconventional hydrocarbon resources in China and the prospect of exploration and development, *Petroleum Exploration and Development*. 39 (2012) 139-146.

- [29] A. Vengosh, R.B. Jackson, N. Warner, T.H. Darrah, A. Kondash, A critical review of the risks to water resources from unconventional shale gas development and hydraulic fracturing in the United States, *Environmental Science & Technology*. 48 (2014) 8334-8348.
- [30] R. Wasylishen, S. Fulton, Reuse of Flowback and Produced Water for Hydraulic Fracturing in Tight Oil, Penn West Exploration, Calgary. (2012).
- [31] M.M. Maricq, S.J. Harris, J.J. Szente, Soot size distributions in rich premixed ethylene flames, *Combustion & Flame*. 132 (2003) 328-342.
- [32] B. Zhao, Z. Yang, J. Wang, M.V. Johnston, H. Wang, Analysis of soot nanoparticles in a laminar premixed ethylene flame by scanning mobility particle sizer, *Aerosol Science & Technology*. 37 (2003) 611-620.
- [33] M.M. Maricq, N. Xu, The effective density and fractal dimension of soot particles from premixed flames and motor vehicle exhaust, *Journal of Aerosol Science*. 35 (2004) 1251-1274.
- [34] B. Zhao, Z. Yang, Z. Li, M.V. Johnston, H. Wang, Particle size distribution function of incipient soot in laminar premixed ethylene flames: effect of flame temperature, *Proceedings of the Combustion Institute*. 30 (2005) 1441-1448.
- [35] A.D. Abid, N. Heinz, E.D. Tolmachoff, D.J. Phares, C.S. Campbell, H. Wang, On evolution of particle size distribution functions of incipient soot in premixed ethylene–oxygen–argon flames, *Combustion & Flame*. 154 (2008) 775-788.
- [36] J. Camacho, C. Liu, C. Gu, H. Lin, Z. Huang, Q. Tang, X. You, C. Saggese, Y. Li, H. Jung, L. Deng, I. Wlokas, H. Wang, Mobility size and mass of nascent soot particles in a benchmark premixed ethylene flame, *Combustion & Flame*. 162 (2015) 3810-3822.
- [37] M. Matti Maricq, Soot formation in ethanol/gasoline fuel blend diffusion flames, *Combustion & Flame*. 159 (2012) 170-180.
- [38] M. Matti Maricq, Physical and chemical comparison of soot in hydrocarbon and biodiesel fuel diffusion flames: A study of model and commercial fuels, *Combustion & Flame*. 158 (2011) 105-116.
- [39] R.J. Santoro, H.G. Semerjian, R.A. Dobbins, Soot particle measurements in diffusion flames, *Combustion & Flame*. 51 (1983) 203-218.
- [40] B. Oger, *Soot characterisation in diesel engines using laser-induced incandescence*, PhD Thesis, University of Brighton, Brighton, United Kingdom, 2012, pp. 216-217. (Publicly available at <http://eprints.brighton.ac.uk/12375>)
- [41] K. Siegmann, H. Hepp, K. Sattler, Reactive dimerization: a new PAH growth mechanism in flames, *Combustion Science & Technology*. 109 (1995) 165-181.
- [42] M. Saffaripour, P. Zabeti, M. Kholghy, M.J. Thomson, An experimental comparison of the sooting behavior of synthetic jet fuels, *Energy Fuels*. 25 (2011) 5584-5593.

- [43] W.C. Hinds, *Aerosol Technology: Properties, Behavior, and Measurement of Airborne Particles*, John Wiley & Sons, 1999, pp. 269-271.
- [44] F.S. Lai, S.K. Friedlander, J. Pich, G.M. Hidy, The self-preserving particle size distribution for Brownian coagulation in the free-molecule regime, *Journal of Colloid Interface Science*. 39 (1972) 395-405.
- [45] M. Frenklach, H. Wang, Detailed modeling of soot particle nucleation and growth, *Symposium (International) on Combustion*. 23 (1991) 1559-1566.
- [46] D. McElreath, Comparison of Hydraulic Fracturing Fluids Composition with Produced Formation Water following Fracturing – Implications for Fate and Transport, in: *Proceedings of the Technical Workshops for the Hydraulic Fracturing Study: Fate and Transport*, U.S. Environmental Protection Agency (US EPA), Arlington, VA, 2011.
- [47] V.N. Balashov, T. Engelder, X. Gu, M.S. Fantle, S.L. Brantley, A model describing flowback chemistry changes with time after Marcellus Shale hydraulic fracturing, *American Association of Petroleum Geology Bulletin* 99 (2015) 143– 154.
- [48] URS Corporation, *Methane Emission Factor Development Project for Select Sources in the Natural Gas Industry Task 1 Report*, 2009.
- [49] C. Clark, J. Veil, *Produced Water Volumes and Management Practices in the United States*, Oak Ridge, TN, 2009.
- [50] P. Gokulakrishnan, A.D. Lawrence, An Experimental Study of the Inhibiting Effect of Chlorine in a Fluidized Bed Combustor, *Combustion & Flame*. 652 (1998) 640–652.
- [51] X. Wei, Y. Wang, D. Liu, H. Sheng, Influence of HCl on CO and NO emissions in combustion, *Fuel*. 88 (2009) 1998–2003.
- [52] X. Wei, X. Han, U. Schnell, H. Wo, K.R.G. Hein, The Effect of HCl and SO₂ on NO_x Formation in Coal Flames, *Energy & Fuels*. 17 (2003) 1392–1398.
- [53] H. Lopes, I. Gulyurtlu, P. Abelha, T. Crujeira, D. Salema, M. Freire, et al., Particulate and PCDD/F emissions from coal co-firing with solid biofuels in a bubbling fluidised bed reactor, *Fuel*. 88 (2009) 2373– 2384.
- [54] L. Lundin, S. Jansson, The effects of fuel composition and ammonium sulfate addition on PCDD, PCDF, PCN and PCB concentrations during the combustion of biomass and paper production residuals., *Chemosphere*. 94 (2014) 20–6.
- [55] J. Aurell, J. Fick, P. Haglund, S. Marklund, Effects of sulfur on PCDD/F formation under stable and transient combustion conditions during MSW incineration., *Chemosphere*. 76 (2009) 767–73.
- [56] G. Yang, I.M. Kennedy, The effect of strain on laminar diffusion flames of chlorinated hydrocarbons, *Combustion & Flame*. 92 (1993) 187–196.

- [57] D. Lentini, Stretched Laminar Flamelet Model of Turbulent Chloromethane-Air Nonpremixed Jet Flames, *Combustion & Flame*. 103 (1995) 328–338.
- [58] M. Xieqi, B. Cicek, S.M. Senkan, Chemical Structures of Fuel-Rich and Fuel-Lean Flames of CCl₄/CH₄ Mixtures, *Combustion & Flame*. 145 (1993) 131–145.
- [59] C. Procaccini, J.W. Bozzelli, J.P. Longwell, K. a. Smith, A.F. Sarofim, Presence of Chlorine Radicals and Formation of Molecular Chlorine in the Post-Flame Region of Chlorocarbon Combustion, *Environmental Science & Technology*. 34 (2000) 4565–4570.
- [60] A.R. Koebele, D.C. Tilotta, Determination of Chlorinated Hydrocarbon Introduced into Air/Acetylene Flames by Fourier Transform Infrared Emission Spectroscopy, *Talanta*. 40 (1992) 247–254.
- [61] H.K. Chelliah, a. K. Lazzarini, P.C. Wanigarathne, G.T. Linteris, Inhibition of premixed and non-premixed flames with fine droplets of water and solutions, *Proceedings of the Combustion Institute*. 29 (2002) 369–376.
- [62] X. Cao, J. Ren, Y. Zhou, Q. Wang, X. Gao, M. Bi, Suppression of methane/air explosion by ultrafine water mist containing sodium chloride additive., *Journal of Hazardous Materials*. 285 (2015) 311–8.
- [63] D.J. Corbin, Methodology and Experiments to Determine Soot and NO_x Yields from a Vertical Lab-Scale Flare Burning Alkane-Mixtures and Ethylene By, Carleton University, 2014.
- [64] V.M. Torres, S. Herndon, E. Wood, F.M. Al-Fadhli, D.T. Allen, Emissions of Nitrogen Oxides from Flares Operating at Low Flow Conditions, *Industrial & Engineering Chemistry Research*. 51 (2012) 12600–12605.
- [65] US EPA, Parameters for Properly Designed and Operated Flares, U.S. Environmental Protection Agency (US EPA) Office of Air Quality Planning and Standard (OAQPS), 2012.
- [66] E. Radloff, Technical Paper NO_x Emissions Reduction Through Water Injection, *Naval Engineers Journal*. 3 (2006) 65– 76.
- [67] W.D. Chang, S.B. Karra, S.M. Senkan, A computational study of chlorine inhibition of CO flames, *Combustion & Flame*. 69 (1987) 113–122.
- [68] J.A. Miller, C.T. Bowman, Mechanism and Modeling of Nitrogen Chemistry in Combustion, *Progress in Energy and Combustion Science*. 15 (1989) 287–338.